Time evolution of gamma rays from supernova remnants

Daniele Gaggero, Fabio Zandanel, Pierre Cristofari, Stefano Gabici

Monthly Notices
of the
ROYAL ASTRONOMICAL SOCIETY

MNRAS **475,** 5237–5245 (2018)
Advance Access publication 2018 January 17

doi:10.1093/mnras/sty140

Time evolution of gamma rays from supernova remnants

Daniele Gaggero,[1]★ Fabio Zandanel,[1] Pierre Cristofari[2] and Stefano Gabici[3]

[1]*GRAPPA, Institute of Physics, University of Amsterdam, NL-1098 XH Amsterdam, the Netherlands*
[2]*Columbia University, 10027 New York, USA*
[3]*APC, Univ. Paris Diderot, CNRS/IN2P3, CEA/Irfu, Obs. de Paris, Sorbonne Paris Cité, F-75013 Paris, France*

Accepted 2018 January 12. Received 2017 December 18; in original form 2017 November 13

ABSTRACT

We present a systematic phenomenological study focused on the time evolution of the non-thermal radiation – from radio waves to gamma rays – emitted by typical supernova remnants via hadronic and leptonic mechanisms, for two classes of progenitors: thermonuclear and core–collapse. To this aim, we develop a numerical tool designed to model the evolution of the cosmic ray spectrum inside a supernova remnant, and compute the associated multi-wavelength emission. We demonstrate the potential of this tool in the context of future population studies based on large collection of high-energy gamma-ray data. We discuss and explore the relevant parameter space involved in the problem, and focus in particular on their impact on the maximum energy of accelerated particles, in order to study the effectiveness and duration of the PeVatron phase. We outline the crucial role of the ambient medium through which the shock propagates during the remnant evolution. In particular, we point out the role of dense clumps in creating a significant hardening in the hadronic gamma-ray spectrum.

Key words: cosmic ray – ISM: supernova remnants.

1 INTRODUCTION

A major goal in the field of high-energy astrophysics is the identification of the Galactic sources able to accelerate hadronic cosmic rays (CRs) all the way up to $\mathcal{O}(PeV)$ energies.

Baade & Zwicky (1934) proposed supernova remnants (SNRs) as candidate sources out of energy budget arguments; the picture was better defined later in terms of SNRs located in our own Galaxy (Ter Haar 1950; Ginzburg 1956; Morrison 1957); however, a physical process able to provide such a powerful CR acceleration at SNR shocks had not been proposed then. Other classes of sources can be at work as well. For example, OB associations may provide a significant contribution, as first noticed in the 1970s (Reeves 1973; Montmerle 1979), and recently pointed out by Murphy et al. (2016) after the measurements of the elemental compositions performed by balloon experiments such as super-TIGER. Despite these recent findings, the SNR paradigm remains the most promising one, and the most widely studied in the literature.

A specific theory for diffusive shock acceleration (DSA) at SNR shocks was developed by Bobalsky[1] (Axford, Leer & Skadron 1977; Krymskii 1977; Bell 1978; Blandford & Ostriker 1978). It was soon understood that PeV energies cannot be reached without a relevant magnetic field amplification at the shock. The physics behind such process is still unclear, and is considered a critical issue in this theoretical framework: see, in particular, Bell (2004), Drury & Downes (2012), Giacalone & Jokipii (2007), and also the very recent discussion presented in Gabici, Gaggero & Zandanel (2016).

In order to shed light on these issues, useful information comes from a careful investigation of the non-thermal multi-wavelength radiation associated with these objects, from radio waves all the way up to X- and gamma rays, as reviewed e.g. in Berezhko (2005), Ellison et al. (2007) and Aharonian (2013).

On the experimental side, we are collecting plenty of multi-wavelength data. The imaging Cherenkov telescopes currently in operation (MAGIC, H.E.S.S., and VERITAS) have detected 16 TeV sources associated with shell-type SNRs;[2] at lower energy, few tens of firm identifications are currently listed in the first *Fermi*-LAT catalogue of SNRs (Acero et al. 2016). However, most of these objects are quite old and none of these show clear evidence of acceleration up to PV rigidities. The only case of a diffuse gamma-ray emission without cutoff in the multi-TeV domain has recently been discovered by H.E.S.S. in the Galactic ridge region (HESS Collaboration et al. 2016). That important result triggered a debate in the community (Gaggero et al. 2017; Jouvin, Lemière & Terrier 2017) about the origin and the nature of the emission.

Among the youngest SNRs observed, the most studied are SN1572 (Tycho's nova, see e.g. the TeV data from Acciari et al. 2011 and the analysis from Morlino & Caprioli 2012), SN1604

★ E-mail: daniele.gaggero@gmail.com

[1] Thierry Montmerle's acronym for Blandford, Ostriker, Bell, Axford, Leer, Skadron, and Krymsky.

[2] http://tevcat.uchicago.edu (Wakely & Horan 2008).

(Kepler's nova, see Vink 2016 for a review), and Cassiopea A (Acciari et al. 2010). All those sources are more than three centuries old and do not show clear evidence for ongoing PeV acceleration of protons. The much younger G1.9+0.3 (Reynolds et al. 2008) is ∼8 kpc away and embedded in the bright Galactic ridge region, so it is difficult to identify its high-energy gamma-ray emission. The youngest known remnant in the Local Group of galaxies, SN1987, is a Type II remnant located even farther away, in the Large Magellanic Cloud (Podsiadlowski 1992), and therefore only future, more sensitive, imaging Cherenkov telescopes such as the Cherenkov Telescope Array (CTA; Actis et al. 2011) will have the opportunity to study its spectrum up to multi-TeV energies.

Despite this wide collection of data, a clear understanding of the crucial aspects of CR acceleration is still missing. The goal of this paper is to provide a systematic study about the evolution of the non-thermal emission from SNRs as a function of time. To this aim, we develop a numerical tool designed to compute the maximum energy of accelerated particles as a function of a well-defined set of free parameters, follow the evolution of CR spectra accordingly, and finally provide a prediction for the radio to gamma-ray spectra at different times. This tool includes a detailed description of the ambient medium where the shock propagates. We pay particular attention to the duration of the PeVatron phase and outline, in this context, the crucial role of the high-density progenitor star wind. Moreover, we discuss how dense clumps may significantly shape the spectrum of the hadronic emission.

The paper is organized as follows. In Section 2 we describe our setup for the time evolution of Type I and II SNRs. In Section 3 we discuss how the maximum energy of hadronic and leptonic acceleration evolves with time. Section 4 presents our framework for the time evolution of the CR spectrum in the remnant. In Section 5 we discuss the resultant broad-band spectra, with particular emphasis on the gamma-ray emission and its time evolution as a function of the free parameters considered. Finally, in Section 6 we present our conclusions.

2 DYNAMICAL EVOLUTION

The typical evolution of a SNR shell is usually divided into three periods: ejecta-dominated, Sedov, and radiative phase. The transition between ejecta-dominated and Sedov phase occurs when swept-up mass becomes comparable to the mass of stellar matter ejected by the supernova event.

We consider and model here the first two, when most of the particle acceleration actually takes place.

For a Type Ia supernova exploding in a homogeneous medium, the time evolution of the radius and velocity of the shock in the ejecta-dominated phase can be written as (Chevalier 1982):

$$R_{\rm s} = 5.3 \left(\frac{E_{51}^2}{M_{\rm ej,\odot} n}\right)^{1/7} t_{\rm kyr}^{4/7}\ {\rm pc}\,, \tag{1}$$

$$u_{\rm s} = 3.0 \times 10^8 \left(\frac{E_{51}^2}{M_{\rm ej,\odot} n}\right)^{1/7} t_{\rm kyr}^{-3/7}\ {\rm cm\,s^{-1}}\,, \tag{2}$$

where E_{51} is the supernova explosion energy in units of 10^{51} erg, $M_{\rm ej,\odot}$ the mass of the ejecta (expressed in solar masses), and n the ISM density (in cm^{-3}). The expressions above are based on the assumption that the ejecta feature a radial power-law density profile $\varrho \propto r^{-k}$ with $k = 7$ (Chevalier 1982). On the other hand, the shock resulting from a Type II supernova initially propagates in the wind of the progenitor star, characterized by a density profile $\varrho_{\rm w} = \dot{M}/(4\pi u_{\rm w} r^2)$ where $\dot{M}$ and $u_{\rm w}$ are the mass-loss rate and the velocity of the wind, respectively. The time evolution of the radius and speed of the SNR shock can then be written as (Chevalier & Liang 1989):

$$R_{\rm s} = 7.7 \left(\frac{E_{51}^{7/2} u_{\rm w,6}}{\dot{M}_{-5} M_{\rm ej,\odot}^{5/2}}\right)^{1/8} t_{\rm kyr}^{7/8}\ {\rm pc}\,, \tag{3}$$

$$u_{\rm s} = 6.6 \times 10^8 \left(\frac{E_{51}^{7/2} u_{\rm w,6}}{\dot{M}_{-5} M_{\rm ej,\odot}^{5/2}}\right)^{1/8} t_{\rm kyr}^{-1/8}\ {\rm cm\,s^{-1}}\,, \tag{4}$$

where $\dot{M} = 10^{-5}\dot{M}_{-5}\ {\rm M_\odot\,yr^{-1}}$ and $u_{\rm w} = 10^6 u_{\rm w,6}\ {\rm cm\,s^{-1}}$ and a density profile of the ejecta with $k = 10$ has been assumed. For completeness, we mention that a simplified description of the ejecta-dominated phase has been often adopted in the literature (see e.g. Finke & Dermer 2012). According to this picture the shock speed is assumed to be constant during most of the ejecta-dominated phase, and determined by:

$$E_{\rm SN} \simeq \frac{1}{2} M_{\rm ej} u_{\rm s}^2\,, \tag{5}$$

where $E_{\rm SN}$ is the supernova explosion energy and $M_{\rm ej}$ the mass of ejecta. The equation captures the fact that, in the very early phase of the evolution of a SNR, almost all the energy is in the form of ejecta kinetic energy. This gives a constant value of the shock speed equal to:

$$u_{\rm s} = 10^9 E_{51}^{1/2} M_{\rm ej,\odot}^{-1/2}\ {\rm cm\,s^{-1}}\,. \tag{6}$$

In the following we will consider both the self-similar scalings given by equations (1)–(4) and the simplified expressions given by equation (6) for estimating the maximum energies attained by electrons and protons (see Fig. 1). However, we adopt only the self-similar scalings of equations (1)–(4) in the further calculation of the evolution of CR spectra and of the corresponding non-thermal radiations.

As far as the Sedov phase is concerned, we adopt the thin-shell approximation. This framework has been often used to describe the SNR dynamical evolution (see e.g. Ostriker & McKee 1988; Bistnovatyi-Kogan & Silich 1995), and is based on the assumption that the mass is mainly concentrated within a spherical shell of negligible thickness located at the forward shock (radial coordinate $r = R_{\rm s}$).

Since radiative processes do not affect the SNR evolution in this phase, the (conserved) total energy is equal to the supernova explosion energy $E_{\rm SN}$, and can be decomposed into the sum of the shell kinetic energy and the SNR thermal energy:

$$E_{\rm SN} = \frac{M u_{\rm s}^2}{2} + \frac{4\pi R_{\rm s}^3}{3}\frac{P_{\rm in}}{\gamma + 1}\,, \tag{7}$$

where γ is the adiabatic index, and M is the sum of swept-up and ejecta mass:

$$M = 4\pi \int_0^{R_{\rm s}} {\rm d}r r^2 \varrho(r) + M_{\rm ej}\,. \tag{8}$$

The equation of momentum conservation reads:

$$\frac{{\rm d}(M u_{\rm s})}{{\rm d}t} = 4\pi R_{\rm s}^2 P_{\rm in}\,, \tag{9}$$

where we assumed that the SNR shock expands in a cold medium characterized by negligible pressure $P_0 \ll P_{\rm in}$.

We want to solve equations (7), (8), and (9), and obtain the evolution of the SNR shock position and velocity until the radiative

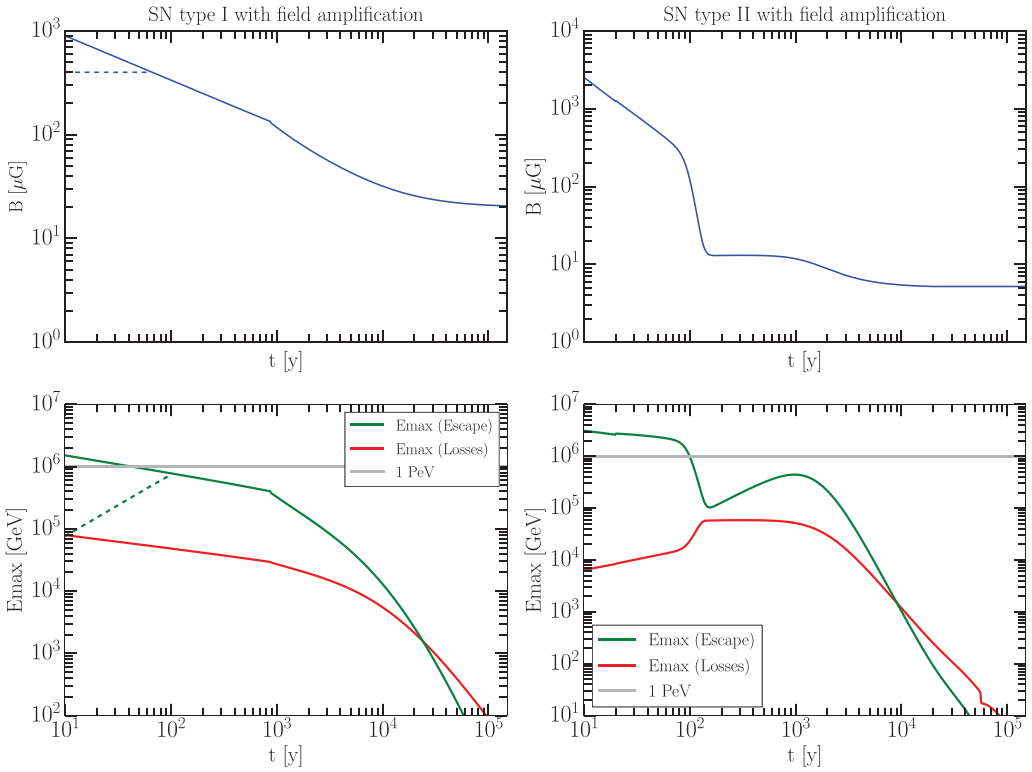

Figure 1. Upper panel: time evolution of the magnetic field strength upstream. Lower panel: maximum energy of accelerated particles. The maximum energy is determined by particle escape (green lines) for protons, and, for the electrons, by the most stringent condition between escape losses (red lines). In the Type Ia case, solid (dashed) lines refer to the choice of equations (1)–(4) (5–6) to describe the ejecta-dominated phase. For the Type II case, the scenario corresponding to equations (5) and (6) does not show any difference with respect to the other one for the range of times we are considering here.

phase, when cooling starts playing a dominant role. To this aim, we fix the explosion energy $E_{\rm SN} = 10^{51} E_{51}$ erg, the ejecta mass $M_{\rm ej}$, and the ambient medium density profile $\varrho(r)$.

As discussed above, for a thermonuclear (Type Ia) supernova we assume the ambient medium to be homogeneous, with a density $\varrho = \mu\, n\, m_{\rm p}$ ($m_{\rm p}$ is the proton mass and $\mu \sim 1.4$ is the average interstellar atom mass in unit of the hydrogen mass). On the other hand, for a core-collapse (Type II) supernova, the SNR shock first propagates through the red supergiant wind characterized by a density profile $\varrho \propto 1/r^2$. After that, in many cases (especially for the most massive progenitors) the shock proceeds across a rarefied bubble created by the wind of the progenitor star during main sequence, and eventually in the interstellar medium (see e.g. Ptuskin & Zirakashvili 2005; Dwarkadas 2011; Cristofari et al. 2013, 2017). The associated length scales can be estimated as follows.

(i) The wind radius $R_{\rm w}$ can be determined by equating the ram wind pressure

$$P_{\rm ram} = \frac{\dot{M} u_{\rm w}}{4\pi r^2} \tag{10}$$

to the thermal pressure in the interior of the bubble (see e.g. Parizot et al. 2004). The typical values one gets are $\mathcal{O}$(pc).

(ii) The radius of the hot bubble is given by

$$R_{\rm b} = 28 (L_{36}/n_0)^{1/5}\, t_{\rm Myr}^{3/5}\ {\rm pc}\,, \tag{11}$$

where L_{36} is the power associated with the main-sequence stellar wind (in units of 10^{36} erg/s), and n_0 the density of the ISM out of the bubble. Following Castor, McCray & Weaver (1975) and Weaver et al. (1977), we adopt

$$n_{\rm b} = 0.01\ \left(L_{36}^{6} n_0^{19} t_{\rm Myr}^{-22}\right)^{1/35}\ {\rm cm}^{-3} \tag{12}$$

for the density inside the bubble, and

$$T_{\rm b} = 1.6 \times 10^{6}\ \left(L_{36}^{8} n_0^{2} t_{\rm Myr}^{-6}\right)^{1/35}\ {\rm K} \tag{13}$$

for the gas temperature.

We are assuming the wind lifetime $t_{\rm Myr}$ to be of the order of several Myr, which corresponds to the duration of the main-sequence phase of very massive stars (Longair 2011).

3 MAXIMUM ENERGY

As mentioned in the Introduction, it is a well-established fact (e.g. Lagage & Cesarsky 1983; Hillas 2005) that CR acceleration up to PV rigidities at SNR shocks requires a relevant amplification of the magnetic field. This consideration is corroborated by several X-ray observations (e.g. Uchiyama et al. 2007; Vink 2012) of young SNRs revealing much larger magnetic fields with respect to the typical interstellar values (of a few μG).

A possible mechanism triggering such intensification of the field was suggested in Bell (2004), based on the idea that magnetic amplification is due to a plasma instability induced by the streaming of CR protons away from shocks. Another scenario (*Drury instability*) was proposed in Drury & Downes (2012). According to this model, the field is significantly amplified by turbulence induced by the CR gradient upstream acting on an inhomogeneous medium.

Since the theoretically predicted efficiency of such processes is still unclear (see e.g. the reference list in Gabici et al. 2016),

here we choose to follow an observation-driven approach: given that young SNR data suggest that a small fraction of the shock pressure is actually converted into (downstream) magnetic pressure, following Völk, Berezhko & Ksenofontov (2005), we assume $\xi_B \sim 3.5$ per cent as a reference value. The reader should of course keep in mind that this is a very uncertain estimate, and that smaller (by a factor of a few) values of ξ_B have been quoted in the literature, based on theoretical studies (e.g. Bell et al. 2013). This parameter will turn out to be crucial in determining the maximum energy of accelerated particles, which scales as $\propto \xi_B^{1/2}$.

We now describe a typical prescription to estimate the maximum energy reachable at SNR shocks as a function of the SNR age. Particles are accelerated at SNRs as the result of repeated cycles around the shock. After each cycle, a test particle gains a momentum (Drury 1983):

$$\frac{\Delta p}{p} = \frac{4}{3}\frac{u_1 - u_2}{v}, \tag{14}$$

where p is the particle momentum, v is its speed, and $u_{1(2)}$ is the fluid velocity upstream (downstream) of the shock measured in the shock rest frame. The time needed to complete a cycle is:

$$\Delta t = \frac{4}{v}\left(\frac{D_1}{u_1} + \frac{D_2}{u_2}\right), \tag{15}$$

expressed as the sum of the up- and downstream residence time of a particle. Here, $D_{1(2)}$ is the particle diffusion coefficient, assumed to be spatially uniform upstream (downstream) of the shock. Shocks are very turbulent environments and thus particle diffusion is likely to proceed at the Bohm rate, $D = (1/3) r_L v$, where $r_L = pc/qB$ is the Larmor radius of a particle in a magnetic field of strength B, and q is the elementary charge. At a strong shock of compression factor $r = u_1/u_2 = 4$, a turbulent magnetic field is compressed, on average, by a factor $\sigma = \sqrt{11}$, implying an instantaneous acceleration rate of:

$$\frac{\mathrm{d}p}{\mathrm{d}t} \simeq 0.11 \frac{u_s^2}{D_1} p\,. \tag{16}$$

Strictly speaking, equation (16) refers to a shock of constant velocity, but following Lagage & Cesarsky (1983) we will use it also in the more general case of a shock with a velocity dependent on time.

It is possible to estimate the maximum energy that DSA can provide by evaluating the most stringent among the following conditions.

(i) *Age constraint*. Equation (16) is integrated up to $t_{\rm age}$ in order to get the maximal energy in absence of energy losses and escape from the source.

(ii) *Escape constraint*. The maximal energy due to particle escape can be determined by equating the diffusion length ahead of the shock

$$l_d = \frac{u_s}{D} \tag{17}$$

to a fraction χ of the shock radius [see e.g. Malkov & Drury (2001) for a review].
We assume here $\chi = 0.05$ as in Ptuskin & Zirakashvili (2005). In that paper, a more realistic assessment of this constraint is presented, based on a computation of the turbulence generation via streaming instability and the different damping processes at work (see also Zirakashvili, Ptuskin & Völk 2008). Such approach is beyond the scope of this paper.

(iii) *Energy loss constraint*. The leptonic acceleration is severely limited by synchrotron losses, taking place at a rate $\mathrm{d}p/\mathrm{d}t|_{\rm synch}$. The maximal energy of the electrons can thus be computed by equating the momentum gain (equation 14) and the momentum loss per cycle, the latter being given by

$$\Delta p\,|_{\rm synch} = \left.\frac{\mathrm{d}p}{\mathrm{d}t}\right|_{\rm synch,1} \Delta t_1 + \left.\frac{\mathrm{d}p}{\mathrm{d}t}\right|_{\rm synch,2} \Delta t_2, \tag{18}$$

where the subscripts (1) and (2) refer to the upstream and downstream regions, respectively, and $\Delta t_i = 4D_i/v u_i$ (see e.g. Vannoni, Gabici & Aharonian 2009).

We stress that the value of the magnetic field at the shock is a crucial parameter. As mentioned above, both observations (see e.g. Völk et al. 2005) and theoretical arguments (see e.g. Bell et al. 2013) suggest that the acceleration of particles at shocks induces an amplification of the field such that a small fraction ξ_B, at the few per cent level, of the shock ram pressure is converted into magnetic pressure downstream of the shock: $\xi_B \varrho u_s^2 = B_2^2/(8\pi)$. This implies that the upstream field is amplified up to a value of:

$$B_1 \approx 43 \left(\frac{\xi_B}{0.035}\right)^{1/2} \left(\frac{n}{\mathrm{cm}^{-3}}\right)^{1/2} \left(\frac{u_s}{1000\ \mathrm{km\,s}^{-1}}\right) \mu\mathrm{G}\,, \tag{19}$$

when the shock speed is larger than

$$u_* = \frac{\sigma B_0}{\sqrt{8\pi \xi_B \varrho}} \approx 0.2 \times 10^8 \left(\frac{n}{\mathrm{cm}^{-3}}\right)^{-1/2} \mathrm{cm\,s}^{-1}\,, \tag{20}$$

where $B_0 \approx 5\,\mu$G is the value of the interstellar magnetic field and we have adopted $\xi_B \approx 0.035$ which has been inferred from observations (Völk et al. 2005). For smaller velocities of the shock the magnetic field amplification is ineffective and $B_1 = B_0$. To describe the diffusion coefficient of particles during this late phase ($u_s < u_*$) we follow the phenomenological approach by Zirakashvili & Ptuskin (2012) and multiply the expression of the Bohm diffusion coefficient by the factor $(1 + (u_*/u_s)^2)^3$, which implies that the diffusion coefficient becomes larger (i.e. particles are less confined) as the shock slows down.

Within this framework, we can compute the maximum energy of particles accelerated at a given SNR at a given time. For protons, the maximum energy is equal to $\min(E_{\rm max}^{\rm age}, E_{\rm max}^{\rm esc})$, while for electrons it is equal to $\min(E_{\rm max}^{\rm age}, E_{\rm max}^{\rm esc}, E_{\rm max}^{\rm syn})$.

The main result, for the default SNIa and SNII scenarios (see parameters in Table 1), is shown in Fig. 1.

The lower panels show the evolution of the maximum energy with time, while the upper panels represent the value of the upstream magnetic field as a function of time. We remark that the age constraint is never relevant in the time-span we are

Table 1. Our benchmark choices for the parameters. The rows refer to: the supernova explosion energy; the ejecta mass; the magnetic field amplification efficiency; the ISM number density (relevant for SNIa); the red supergiant wind mass-loss rate and velocity, the ISM number density in the cavity (relevant for SNII); the ratio between magnetic and total energy inside the remnant $\xi_{\rm inside}$. All quantities are expressed in normalized units as in the main text.

Parameter	Type Ia	Type II
E_{51}	1	1
$M_{\rm ej,\odot}$	1.4	3
ξ_B	3.5 per cent	3.5 per cent
n	0.1	–
$\dot{M}_{-5}$	–	2
$u_{\rm w,6}$	–	1
$n_{\rm cavity}$	–	0.01
$\xi_{\rm inside}$	0.001	0.001

considering, therefore the corresponding line is not shown in the plot. The maximum energy for the protons, which do not suffer from IC and synchrotron energy losses, is thus simply given by $E_{\rm max}^{\rm esc}$ (green line), while – for the leptonic component – the most stringent constraint between $E_{\rm max}^{\rm esc}$ and $E_{\rm max}^{\rm loss}$ applies.

The plots clearly outline, in agreement with previous findings (e.g. Bell et al. 2013), the capability of a typical Type II remnant to sustain a PeVatron phase during the first few decades of its evolution, when the shock is still very fast and is propagating in the thickest part of the wind, thus triggering a highly effective magnetic field amplification.

Regarding Type II remnants, we also remark how the structure of the ambient medium described above shapes the time evolution of both $E_{\rm max}^{\rm esc}$ and $E_{\rm max}^{\rm loss}$. In particular, the transition between the thick supergiant wind and the cavity is clearly visible at $\simeq 1$ century, and the second transition between cavity and ISM can be identified by the feature at $\simeq 8 \times 10^4$ yr in the $E_{\rm max}^{\rm loss}$ evolution (red line).

4 TIME EVOLUTION OF THE COSMIC RAY SPECTRUM

In this section we describe our model for the time evolution of CR hadrons and leptons inside a typical SNR.

We simulate the SNR evolution for $\sim 10^5$ yr, adopting a time-step of $\simeq 1$ yr. Electrons and protons are injected following an unbroken power law

$$Q = Q_0 E^{-\alpha}, \tag{21}$$

up to $E_{\rm cut}$, where we fix $\alpha = 2.3$.

We remind the reader that, as far as protons are concerned, the escape-limited constraint dominates, while, for the leptons, the minimum between the loss-dominated and escape-dominated $E_{\rm max}$ must be taken into account. For the normalization term of the protons, Q_0, we adopt 10 per cent of the incoming energy flux f, defined as $f = \frac{1}{2}\rho u_{\rm s}^3 \cdot 4\pi R_{\rm s}^2$. We will define later the normalization term for the electrons through the electron-to-proton fraction $K_{\rm ep}$.

We solve the equations describing the time evolution of the CR spectrum inside the remnant with numerical methods, following Finke & Dermer (2012):

$$Q(E,t) = \frac{\partial N(E,t)}{\partial t} + \frac{\partial}{\partial E}\dot{E}N(E,t) \tag{22}$$

where

(i) for the protons, $\dot{E}$ is simply the adiabatic loss term $\dot{E} = k_{\rm ad} E/t$, with $k_{\rm ad} = 1$;

(ii) for the electrons, besides adiabatic losses, we consider the dominant loss terms due to synchrotron emission and inverse-Compton (IC) scattering on the CMB photons (Finke & Dermer 2012).

The equation is discretized on a two-dimensional grid – with logarithmic spacing in energy and a linear binning in time – exploiting a second-order implicit scheme in order to get a stable solution for a wide range of time-steps (see e.g. the discussion in Evoli et al. 2017 about the accuracy of this scheme in the context of CR energy losses.).

In order to mimic the loss of particles upstream, when the escape condition $l_D > \chi R_{\rm shock}$ discussed above is satisfied, we introduce *a posteriori*:

(i) In the hadronic case, an exponential cutoff at $E_{\rm max}$(escape) for each time-step i.[3]

(ii) In the leptonic case, a super-exponential cutoff at $E_{\rm max}$(loss), when synchrotron losses dominate, and an exponential cutoff at $E_{\rm max}$(escape) at late times, when escape is most relevant (see Fig. 1).

As far as the electron evolution is concerned, a key role is played by the synchrotron energy-loss rate, which depends on the average magnetic field inside the remnant $B_{\rm inside}$. We assume here that the magnetic energy is actually a tiny fraction (0.1 per cent) of the total internal energy, and we compute such energy as follows:

(i) During the early ejecta-dominated phase, the internal energy is obtained by integrating the self-similar pressure profiles from Chevalier (1982), and then applying the equation of state $\epsilon = 3P/2$.

(ii) In the Sedov phase, we assume that thin-shell approximation holds and simply exploit energy conservation:

$$E_{\rm int} = E_{\rm SN} - \frac{M u_{\rm S}^2}{2}, \tag{23}$$

where we set $E_{\rm SN} = 10^{51}$erg; M is the total mass (swept + ejecta).

In general, we interpolate between the two extreme cases.

With this procedure we compute the mean magnetic field within the remnant, and hence the synchrotron energy-loss rate for the electrons. The final outcome of the computation is the predicted time evolution of the electron and proton spectra. We remark that a clear *cooling break* naturally appears in the leptonic spectra. The position of this spectral feature is consistent with the theoretical prediction, i.e. $E_{\rm break}(t) \simeq k_{\rm synch} t$.

4.1 Evolution in a clumpy medium

When considering the case of Type II supernovae, we additionally model the possibility that the SNRs expand in a clumpy medium. In this case, the spectrum of protons locked in clumps is much harder than the one obtained at the shock with the consequence that hadronic emission can result in harder spectra, similar to that typically obtained leptonically [see Gabici & Aharonian (2014) and references therein].

The interaction of the SNR shock with clumps can be modelled as follows (see e.g. Gabici & Aharonian 2014, for an extensive description of the procedure). We consider that the SNR shock is evolving in a clumpy medium where the clump density is $n_{\rm clump} \approx 3\,{\rm pc}^{-3}$, and the gas density inside each clump is typically $10^3\,{\rm cm}^{-3}$. Once a clump enters the SNR shock, it is bombarded by the CR contained in the SNR shell, and the evolution of the total CR content inside the clump $N_{\rm cl}$ is described by the equation:

$$\frac{\partial N_{\rm cl}(E)}{\partial t} = \frac{(V_{\rm cl}/V_{\rm s})N_{\rm CR}(E) - N_{\rm cl}(E)}{\tau_{\rm d}}, \tag{24}$$

where $N_{\rm CR}$ is the CR spectrum inside the SNR shell, $V_{\rm cl}$ and $V_{\rm s}$ are, respectively, the volumes of the clump and of the SNR shell filled with CRs, and $\tau_{\rm d}$ the time needed for a CR to diffusive into a clump. $V_{\rm cl}$ is estimated by assuming a spherical shape of radius $L_{\rm c} = 0.1$ pc. $V_{\rm s}$ is calculated considering most of the CR content remain between the forward shock $R_{\rm s}$ and the contact discontinuity at $\approx 0.9\,R_{\rm s}$. The

[3] For the protons, we expect the maximum energy to be given by $E_{\rm max}$(escape) for most of the evolution, and to be monotonically decreasing with time. Therefore, this prescription correctly accounts for the fact that PeV protons accelerated in the early stages are lost during the subsequent evolution, when the magnetic field is lower and the Larmor radius is larger.

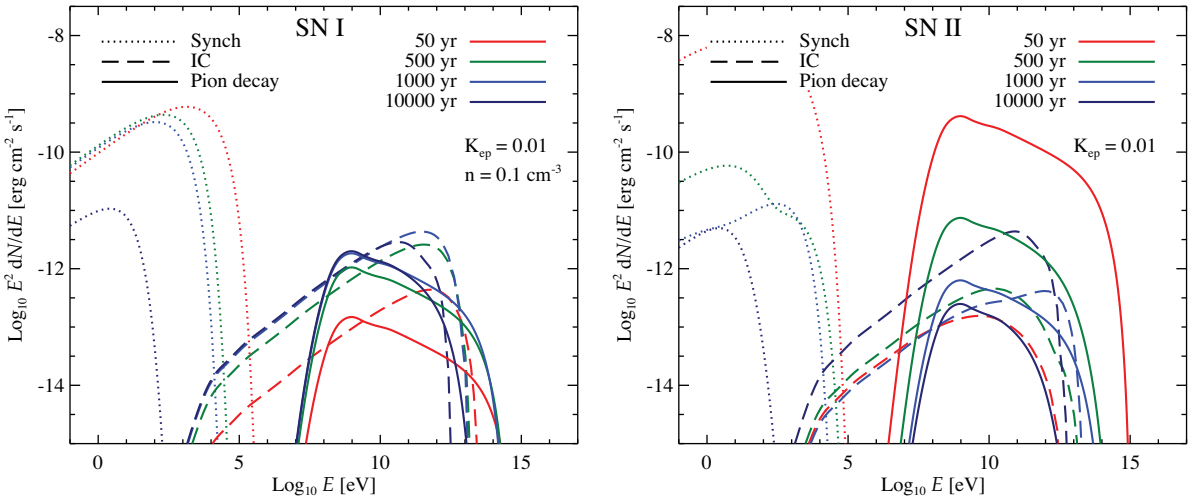

Figure 2. Time evolution of the non-thermal spectra emitted by a Type I and II SNR for our benchmark setups.

penetration time τ_d can be estimated by considering that the diffusion of CRs in the very turbulent structure of the surrounding of the clumps is of the Bohm type and writing $\tau_d \approx L_{tr}^2/6D_B$ where $L_{tr} = 0.05$ pc is the thickness of the layer surrounding the clump and D_B the Bohm diffusion coefficient.

5 GAMMA-RAY SPECTRA AND EVOLUTION

We present here the results for the evolution of the non-thermal emission associated with Type I and Type II SNRs (assuming they are located at 2 kpc distance). Once we have modelled the evolution of the electron and proton spectra within the framework presented above, we determine the corresponding synchrotron, IC and pion-decay spectra.

The synchrotron and IC spectra are computed following Blumenthal & Gould (1970). The magnetic field we consider for the computation of the synchrotron spectrum is the average magnetic field within the remnant B_{inside}. The scattered photon field for the IC computation is the inter-stellar radiation field including the cosmic microwave background (CMB), and the infrared, stellar, and UV light, for which we use the analytical approximation of Delahaye et al. (2010), based on the model described in Porter & Strong (2005); in particular, we use the model M1 of their table 2. We remark that the CMB and the infrared components dominate the IC emission. The computation of the pion-decay gamma-ray spectrum is done (Kafexhiu et al. 2014) with the NAIMA package (Zabalza 2015). In this case, at each time-step, the target density for the hadronic collisions is taken to be the swept-up mass as if it were enclosed in a shell at 0.9–1 R_s.

In Fig. 2, we consider two benchmark cases for the evolution of a Types Ia and II SNR. We refer again to Table 1 for the list of the main parameters. In particular, for our benchmark cases, we assume $n = 0.1\,\mathrm{cm}^{-3}$ as interstellar medium density for the Type Ia SNR, and we adopt an electron-to-proton fraction of $K_{ep} = 0.01$. Several reference ages are considered in the plot: 50 yr, 500 yr (compatible with the age of *Cas A*), 10^3 yr (compatible with the age of RX J1713.7−3946), and 10^4 yr (when the SNR is expected to be at the end of the Sedov phase). The spectral shapes of the synchrotron, IC and pion emission are clearly recognizable in the figure.

We point out two crucial aspects.

(i) The well-known feature below the π^0 mass scale associated with hadronic emission, usually called *pion bump*. The importance of this feature mainly depends on the ratio between the electron and proton number density (K_{ep}), and the gas density of the surrounding medium. For our reference choice ($n = 0.1\,\mathrm{cm}^{-3}$, $K_{ep} = 0.01$), the pion bump is barely visible on top of the IC emission for the Type Ia SNR, likely not enough to be identified observationally. However, for the Type II SNR, the pion-decay emission largely dominates over the IC at early stages, become comparable, but with a rather different spectrum, around 10^3 yr, and eventually sub-dominant at the latest stages.

(ii) The high-energy cutoff and its time evolution. We find that a typical SNR – for the default values of the parameters considered here – is a bright gamma-ray source up to energies consistent with a CR population that extends up to PeV (i.e. a *PeVatron*) during the early stage of its evolution, until ∼100 yr. This result agrees with what we showed in the previous sections. We also note that some minor features can be appreciated in the synchrotron and IC spectra of the Type II SNR in the right panel of Fig. 2 – these can be traced back to the shape of our evolving electron spectrum.

We now turn our attention to the impact of the most relevant parameters on these features.

In Fig. 3, we show how the pion bump in the Type Ia SNR is highly enhanced, and, conversely, strongly suppressed, for values of the interstellar gas density as large as $1\,\mathrm{cm}^{-3}$, and values of K_{ep} as low as 10^{-5}, respectively.

The presence of the PeVatron phase, and its duration, is instead obviously liked to the maximal energies reached by the protons. In our computation of E_{max} we rely on the assumption that a fraction ξ_B of the shock ram pressure $P_{ram} = \rho(r)u_w(r)$ gets converted into magnetic energy. Therefore, the maximum energy mainly depends on the value of the gas density in the interstellar medium around the remnant, and on the value of ξ_B itself, which still remains an open issue (Giacalone & Jokipii 2007; Drury & Downes 2012; Bell et al. 2013). In Fig. 4, we investigate in particular the dependence on the gas density around the SN event, which in turn depends on $\dot{M}$. We find that the SNR is not a PeVatron, even at very early times, for values of $\dot{M}$ lower than $\sim 10^{-5}\,\mathrm{M}_\odot\,\mathrm{yr}^{-1}$ (being $2 \times 10^{-5}\,\mathrm{M}_\odot\,\mathrm{yr}^{-1}$ our benchmark value), while for higher values it safely attains the PeVatron phase up to ∼100 yr (see Smith 2014 for a comprehensive review on the mass-loss rates in different types of progenitor stars.).

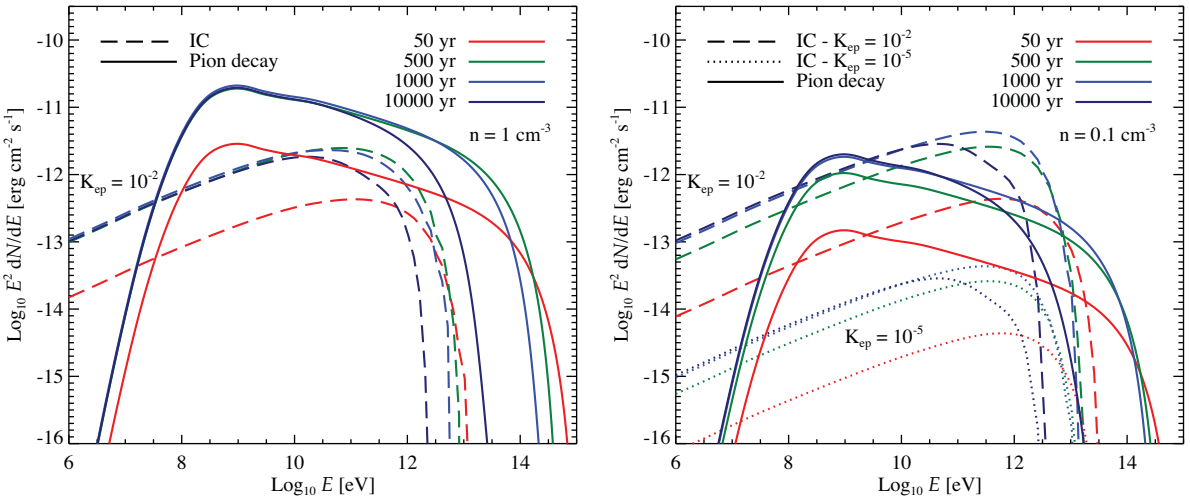

Figure 3. Impact of the interstellar gas density and K_{ep} on the emission from a Type Ia SNR.

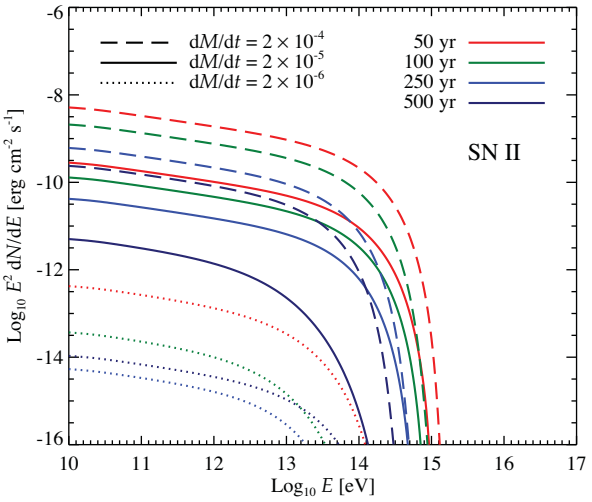

Figure 4. Impact of $\dot{M}$ on the evolution of the spectra of Type II SNRs.

Let us now discuss the role of clumps. In the left panel of Fig. 5, we show the effect of the evolution in a clumpy medium, as described in Section 4.1, for the benchmark case of our Type II SNR. The key feature in this case is that the resultant pion-decay gamma-ray spectra are much harder than the clumpy-free ones, mimicking the spectra typically obtainable with IC emission, and even harder for our parameter choices. We stress this point again in the right panel of Fig. 5, where we try to visualize the trend suggested by current observations of young IC-dominated and old pion-decay-dominated SNRs – see e.g. fig. 6 in Funk (2015) – for the case of our Type II SNR. In this figure, we re-normalized arbitrarily the different spectra at different ages to roughly peak at the same value for visual purposes. In particular, we show the IC and pion-decay emission at 2000 and 10^4 yr as representative of a typical young and middle-age SNR, respectively. We then over-plot the pion-decay emission for a SNR evolving in a clumpy medium and see that this can well mimic the classical shape of an IC spectrum.

As a final discussion point, we compute the photon spectral indexes for our benchmark cases for the IC and pion-decay emission in the 1–100 GeV and 0.5–5 TeV energy ranges. We show the

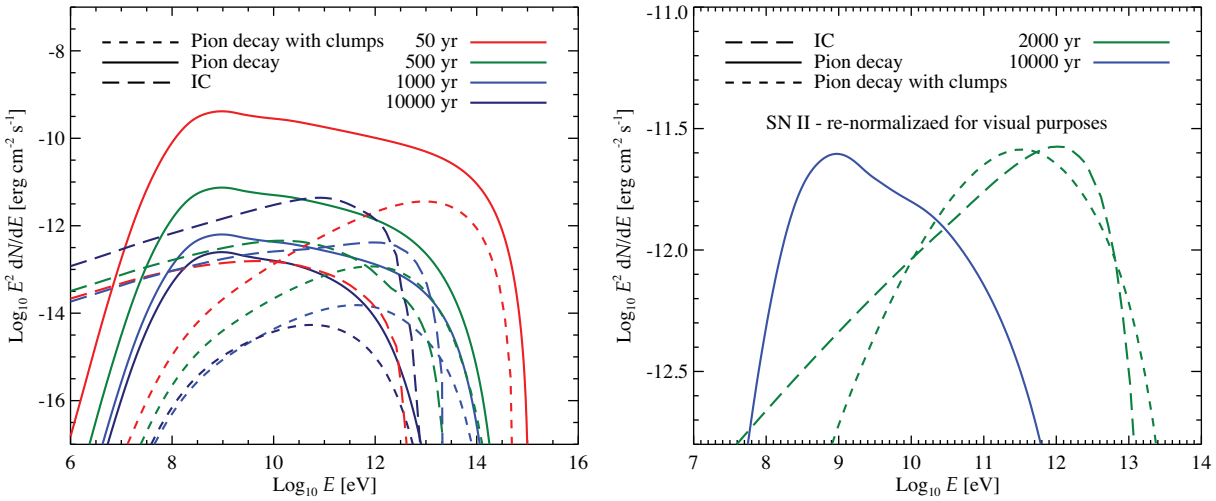

Figure 5. Impact of the presence of clumps on the evolution of the spectra of Type II SNRs on the left, and representation of the observed trend of young-IC-dominated and old-pion-decay-dominated SNRs on the right (see main text for details).

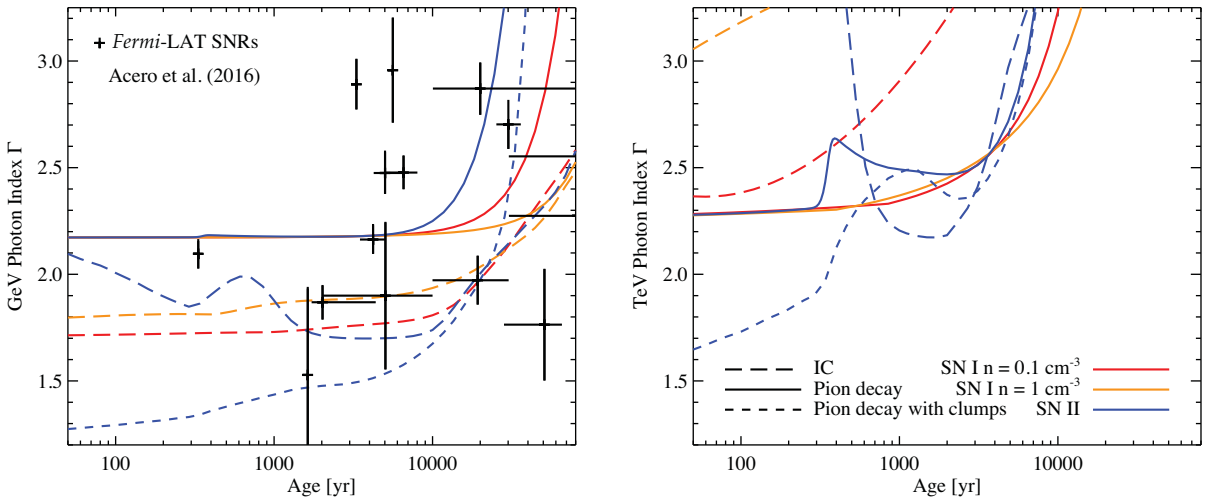

Figure 6. Evolution of the 1–100 GeV (left) and 0.5–5 TeV (right) photon spectral index of IC and pion-decay emissions of Type Ia and II SNRs. The legend for the curves shown in the right panel applies also to the left panel.

resulting trends in Fig. 6. We remind the reader that our injected electron and proton spectral index is $\alpha = 2.3$ (see Section 4), changing this to, e.g. $\alpha = 2.1$ does not change much the trends in Fig. 6 but for an overall shift downward of about 0.1 and 0.2 in photon index for IC and pion-decay emission, respectively. The two panels for the GeV and TeV photon spectral index allow the reader to visualize in a more complete way the spectral evolution at all times. The left panel of Fig. 6 shows the evolution with time of the GeV photon index for our benchmark cases. We notice a regular behaviour, consistent with what we have found so far. In particular, the features clearly visible in the evolution of the Type II SNRs can be easily traced back to the discussion in Sections 2 and 3, and shown in Fig. 1. The same is true for the left panel where the TeV photon index behaviours are shown. These are, in general, less regular and not as obviously interpreted, but we can do so keeping in mind the IC and pion-decay spectra at these energies which are, for most of the considered time-steps, on the edge of the emissions cutoff. This can indeed be seen in both panels: a rapidly growing photon spectral index means that the energies at which we are fitting for it are falling beyond the emissions cutoff. The behaviours for the Type II SNRs are particularly interesting also at TeV energies, where we can clearly appreciate the importance of the IC component around 10^3 yr. The effect of the evolution in a clumpy medium discussed above is clear here both at GeV and TeV energies: the photon spectral indexes of the pion-decay component can be similar, or even harder, than the ones of the IC component for most of the considered time-steps.

In the left panel of Fig. 6, we show the data points corresponding to the SNRs in the first *Fermi*-LAT Supernova Remnant Catalogue (Acero et al. 2016; see their fig. 16) but excluding those classified as interacting with molecular clouds as our current set-up does not model such phase. We show these only for completeness as not much can be deduced from such a comparison at the current observational stage. For the same reason, we do not include TeV data points in the right panel as most of the TeV SNRs are interacting with molecular clouds and/or have larger uncertainties in the spectral indexes. However, future more complete and accurate observational samples both from *Fermi*-LAT, and hopefully its successors (see e.g. De Angelis et al. 2017), and from CTA (Actis et al. 2011; Cristofari et al. 2017) will make such comparisons a powerful tool.

6 SUMMARY

In this paper we studied the time evolution of the (hadronic and leptonic) CR spectrum inside a typical Type Ia and Type II SNR, and computed the associated evolution of the non-thermal emission.

We developed a complete numerical framework mainly inspired by phenomenological considerations. The key ingredient is a significant field amplification. Motivated by the available X-ray observations of young SNRs, we modelled this process by assuming that a small, constant portion ($\simeq 3.5$ per cent) of the energy flux entering the remnant during the expansion of the shock wave is effectively converted into magnetic energy.

We followed the evolution of two benchmark cases, representative of a typical SNIa and SNII, and parametrized the problem in order to allow scans over the relevant parameter space.

We focused on several key aspects. The relevance and duration of the PeVatron phase, the role of the clumpiness of the ambient medium, and the relevance of the characteristic *pion bump* feature in the gamma-ray spectrum, a widely used indicator of the hadronic origin of the gamma-ray emission.

We found that a SNII can sustain the PeVatron phase for several decades, during the early phase of its evolution, due to the combined effects of the large shock velocity and the high density of the ambient medium. The shock propagates in the thick progenitor wind and the magnetic field amplification, linked to the incoming flux of particles, is particularly effective. We discussed how the duration of the PeVatron phase depends on the parameters involved in the problem.

We then computed the gamma-ray spectra at different times, and pointed out how the *pion bump* feature is affected by the largely unknown ratio between the number of accelerated electrons and protons, and by the properties of the ambient medium.

We finally turned our attention to the role of clumps, and outlined their crucial role in shaping the gamma-ray spectrum. In particular, as a consequence of the easier penetration of high-energy CRs inside the densest clumps, we found a significant hardening of the hadronic emission from SNRs exploding in a clumpy medium, and explicitly showed the subsequent degeneracy between hadronic and leptonic spectra especially in middle-aged remnants.

Our numerical framework appears suitable for systematic scans of the parameter space and population studies, and will be useful

in the prospect of a more complete collection of multi-wavelength data, in particular in the TeV domain, that will be provided in the following years by CTA. As a preliminary step, we provided a comparison between the predicted time evolution of the GeV gamma-ray spectral index and the current collection of available data, and presented the expected time evolution of the TeV slope.

ACKNOWLEDGEMENTS

We thank D. Caprioli and the anonymous referee for useful comments and suggestions. SG acknowledges support from the Observatory of Paris (Action Fédératrice CTA) and from the Programme National Hautes Energies (PNHE) funded by CNRS/INSU- IN2P3, CEA and CNES, France. This work was supported by the Netherlands Organization for Scientific Research (NWO) through a Veni grant (FZ).

REFERENCES

Acciari V. A. et al., 2010, ApJ, 714, 163
Acciari V. A. et al., 2011, ApJ, 730, L20
Acero F. et al., 2016, ApJS, 224, 8
Actis M. et al., 2011, Exp. Astron., 32, 193
Aharonian F. A., 2013, Astropart. Phys., 43, 71
Axford W. I., Leer E., Skadron G., 1977, Proc. Int. Cosmic Ray Conf., 11, 132
Baade W., Zwicky F., 1934, Proc. Natl. Acad. Sci., 3, 79
Bell A. R., 1978, MNRAS, 182, 147
Bell A. R., 2004, MNRAS, 353, 550
Bell A. R., Schure K. M., Reville B., Giacinti G., 2013, MNRAS, 431, 415
Berezhko E. G., 2005, Adv. Space Res., 35, 1031
Bisnovatyi-Kogan G. S., Silich S. A., 1995, Rev. Mod. Phys., 67, 661
Blandford R. D., Ostriker J. P., 1978, ApJ, 221, L29
Blumenthal G. R., Gould R. J., 1970, Rev. Modern Phys., 42, 237
Castor J., McCray R., Weaver R., 1975, ApJ, 200, L107
Chevalier R. A., 1982, ApJ, 258, 790
Chevalier R. A., Liang E. P., 1989, ApJ, 344, 332
Cristofari P., Gabici S., Casanova S., Terrier R., Parizot E., 2013, MNRAS, 434, 2748
Cristofari P. et al., 2017, MNRAS, 471, 201
De Angelis A. et al., 2017, Exp. Astron., 44, 25
Delahaye T., Lavalle J., Lineros R., Donato F., Fornengo N., 2010, A&A, 524, A51
Drury L. O'C., 1983, Phys. Rep., 46, 973
Drury L. O'C., Downes T. P., 2012, MNRAS, 427, 2308
Dwarkadas V. V., 2011, Mem. Soc. Astron. Ital., 82, 781
Ellison D. C., Patnaude D. J., Slane P., Blasi P., Gabici S., 2007, ApJ, 661, 879
Evoli C., Gaggero D., Vittino A., Di Bernardo G., Di Mauro M., Ligorini A., Ullio P., Grasso D., 2017, JCAP, 02, 015
Finke J. D., Dermer C. D., 2012, ApJ, 751, 65
Funk S., 2015, Annu. Rev. Nucl. Part. Sci., 65, 245
Gabici S., Aharonian F. A., 2014, MNRAS, 445, L70
Gabici S., Gaggero D., Zandanel F., 2016, preprint (arXiv:1610.07638)
Gaggero D., Grasso D., Marinelli A., Taoso M., Urbano A., 2017, Phys. Rev. Lett., 119, 031101
Giacalone J., Jokipii J. R., 2007, ApJ, 663, L41
Ginzburg V. L., 1956, Nuovo Cimento, 3, 38
HESS Collaboration et al., 2016, Nature, 531, 476
Hillas A. M., 2005, J. Phys. G: Nucl. Part. Phys., 31, R95
Jouvin L., Lemière A., Terrier R., 2017, MNRAS, 467, 4622
Kafexhiu E., Aharonian F., Taylor A. M., Vila G. S., 2014, Phys. Rev. D, 90, 123014
Krymskii G. F., 1977, Akademiia Nauk SSSR Doklady, 234, 1306
Lagage P. O., Cearsky C., 1983, A&A, 125, 249
Longair M. S., 2011, High Energy Astrophysics. Cambridge Univ. Press, Cambridge
Malkov M. A., Drury L. O., 2001, Rep. Progress Phys., 64, 429
Montmerle T., 1979, ApJ, 231, 95
Morlino G., Caprioli D., 2012, A&A, 538, A81
Morrison P., 1957, Rev. Modern Phys., 29, 235
Murphy R. P. et al., 2016, ApJ, 831, 148
Ostriker J. P., McKee C. F., 1988, Rev. Mod. Phys., 60, 1
Parizot E., Marcowith A., van der Swaluw E., Bykov A. M., Tatischeff V., 2004, A&A, 424, 747
Podsiadlowski P., 1992, PASP, 104, 717
Porter T. A., Strong A. W., 2005, Proc. Int. Cosmic Ray Conf., 4, 77
Ptuskin V. S., Zirakashvili V. N., 2005, A&A, 429, 755
Reeves H., 1973, Proc. 13th Int. Cosmic Ray Conference, Vol. 5, Denver, p. 3323
Reynolds S. P. et al., 2008, ApJ, 680, L41
Smith N., 2014, ARA&A, 52, 487
Ter Haar D., 1950, Rev. Modern Phys., 22, 119
Uchiyama. Y., Aharonian F. A., Tanaka. T., Takahashi T., Maeda Y., 2007, Nature, 449, 576
Vannoni G., Gabici S., Aharonian F. A., 2009, A&A, 497, 17
Vink J., 2012, A&AR, 20, 49
Vink J., 2016, preprint (arXiv:1612.06905)
Völk H. J., Berezhko E. G., Ksenofontov L. T., 2005, A&A, 433, 229
Wakely S. P., Horan D., 2008, Proc. Int. Cosmic Ray Conf., 3, 1341
Weaver R., McCray R., Castor J., Shapiro P., Moore R., 1977, ApJ, 218, 377
Zabalza V., 2015, Proc. Int. Cosmic Ray Conf., 34, 922
Zirakashvili V. N., Ptuskin V. S., 2012, Astropart. Phys., 39, 12
Zirakashvili V. N., Ptuskin V. S., Völk H. J., 2008, ApJ, 678, 255

This paper has been typeset from a TEX/LATEX file prepared by the author.